

1
2
3
4
5
6
7
8
9
10
11
12
13
14
15
16
17
18
19

Towards retrieving distributed aquifer hydraulic parameters from distributed strain sensing

Yi Zhang^{1,2*}, Xinglin Lei³, Tsutomu Hashimoto^{1,2}, Ziqiu Xue^{1,2}

Corresponding author: zhangyi@rite.or.jp

¹ Geological Carbon Dioxide Storage Technology Research Association, 9-2, Kizugawadai, Kizugawa-Shi, Kyoto, 619-0292 Japan.

² Research Institute of Innovative Technology for the Earth (RITE), 9-2, Kizugawadai, Kizugawa-Shi, Kyoto, 619-0292 Japan.

³ Geological Survey of Japan, National Institute of Advanced Industrial Science and Technology, AIST Central #7, Higashi 1-1-1, Tsukuba, Ibaraki 305-8567, Japan.

Key Points:

- Small poroelastic deformation during aquifer testing was monitored using a high-resolution distributed strain sensing (DSS) tool.
- DSS data are used to inversely estimate the vertical profiles of permeability and compressibility through a coupled hydromechanical model.
- DSS and inverse modeling are useful for subsurface reservoir characterization and management.

20 Abstract

21 Subtle elastic rock deformation during aquifer testing may bear hydraulic parameter (permeability
22 and compressibility) information owing to the poroelastic hydromechanical coupling effect. Here
23 we report that such in situ rock deformations ($\sim 50 \mu\epsilon$) during an aquifer pumping test are
24 successfully measured along a vertical well by a high-resolution fiber optic distributed strain
25 sensing (DSS) tool with an accuracy of $0.5 \mu\epsilon$. We investigate the feasibility of hydraulic
26 parameter estimation at meter scale using DSS data through a coupled hydromechanical model.
27 Both synthetic and field cases are tested with sensitivity analysis. The results indicate that the
28 simultaneous estimation of permeability and compressibility using DSS data is possible at low
29 noise levels. However, only non-global near-optimal solutions can be obtained using the applied
30 gradient-based inversion algorithm, because of parameter crosstalk and sensitivity problems when
31 the data contain large noise. In particular, estimation is difficult for zones with relatively low
32 permeability due to the low sensitivity to the strain changes. The estimated
33 permeability/compressibility structures for the field test are largely consistent with other
34 geological information from well logs. Our study suggests that DSS data can be quite useful in
35 aquifer characterization and fluid flow profiling in addition to geomechanical monitoring. The
36 obtained hydraulic information is beneficial for the optimized reservoir management of water and
37 oil/gas storage.

38 Plain Language Summary

39 Permeability and compressibility are the two most important hydraulic parameters used in
40 reservoir models for understanding fluid flow behavior. The parameters control the evolution of
41 pore pressure, fluid flow, and coupled deformation in the reservoir. The resultant strain records
42 may contain the information of pore pressure and fluid flow. In this study, we tested the
43 feasibility of simultaneously estimating permeability and compressibility of a multi-layered

44 aquifer using the distributed strain data and a hydromechanically coupled model. The results
45 show that the compressibility and permeability of zones with high permeability can be generally
46 well resolved in the estimation, for they have higher sensitivity to the strain changes, whereas the
47 permeability of zones with relatively lower permeability cannot be well constrained because of
48 the low sensitivity to strain changes. Using the high-fidelity field records of distributed strain data
49 (with an accuracy of $0.5 \mu\epsilon$) in the aquifer pumping test, we constructed the profiles of
50 permeability and compressibility, which are largely consistent with other geological information.
51 Our study provides a new method for reservoir characterization and is useful for optimized
52 reservoir management.

53

54 **1 Introduction**

55 Permeability and compressibility (or hydraulic conductivity and specific storage) are two
56 of the most important hydraulic parameters for modeling fluid flow behavior in underground
57 reservoirs (Anderson et al., 2015; Bear & Verruijt, 2012). A better understanding of the spatial
58 distribution of hydraulic parameters can facilitate more manageable and optimized operations for
59 these utilizations (Miller et al., 2017). Moreover, the parameters are essential for understanding
60 the scale of hydromechanical responses and its role in fluid injection induced seismicity
61 (Guglielmi et al., 2020; Jiang et al., 2020; Shirzaei et al., 2016; Verdon et al., 2015; Keranen et
62 al., 2014; Lei et al., 2020). Hydrogeologists have long pursued an understanding of the spatial
63 structure of hydraulic parameters in aquifer formation. These efforts can be classified into three
64 categories: (1) hydraulic methods; (2) geophysical methods; and (3) geodetic deformation-based
65 methods.

66 The first category includes hydraulic pumping, slug, tracer, and hydraulic tomographic
67 testing methods (Istok & Dawson, 2014; Yeh & Liu, 2000). Among the methods, the pumping

68 test is suggested to be the most reliable method for determining aquifer permeability and
69 compressibility. However, usually only a pair of permeability and compressibility values of the
70 entire aquifer section can be obtained. Beside purposed pumping tests, even natural tidal force
71 induced hydraulic response can be used for parameter estimation (e.g. Hsieh et al., 1987; Wang et
72 al., 2018). The hydraulic tomography (HT) method is a tomographic approach that inversely
73 reconstructs parameter fields using information from multiple hydraulic head (or pressure)
74 records. The promising performance of HT has been documented in many studies even for
75 heterogeneous aquifers (Gottlieb & Dietrich, 1995; Hochstetler et al., 2016; Jiménez et al., 2015;
76 Vasco, 2018; Vasco et al., 2019). However, the method performance greatly depends on data
77 acquisition and the quality of the assumed geostatistical priors (Kitanidis, 1997). Because of the
78 spatial limitation in hydraulic head measurements, the inverted parameter field is often overly
79 smoothed and the model assessment for determining model resolution is required (Aster et al.,
80 2018; Menke, 2018; Vasco et al., 1997). The second category of methods indirectly provides
81 permeability or compressibility data from geophysical parameters, such as electrical resistivity,
82 temperature, or acoustic velocity that are obtained from well logging, cross-well or surface
83 geophysical surveys (Huntley, 1986; Yamamoto et al., 1995). These geophysical parameters
84 usually have a relatively weak physical-constrained relationship with hydraulic parameters. The
85 estimation might be less quantitative compared with the first category. A joint inversion of multi-
86 physical data has been used to give a better parameter characterization (e.g. Commer et al., 2020;
87 Jardani & Revil 2009; Liang et al., 2016).

88 With the advance of space observation technologies, a third category of methods, based on
89 the geodetic observations of earth surface deformations, have been developed to constrain or
90 estimate hydraulic parameters on a large scale. For example, the interferometric synthetic-
91 aperture radar (InSAR) technique and Global Navigation Satellite System (GNSS) method have
92 been applied to monitor the surface deformation caused by underground fluid extractions or

93 injections and obtain the lateral permeability distribution of underground reservoirs over a large
94 area (Alghamdi et al., 2020; Bohloli et al., 2018; Comola et al., 2016; Shirzaei et al., 2019; Vasco
95 et al., 2008, 2010). Despite the progress made, to date, it remains a challenge to characterize fine-
96 scale hydraulic parameters in the vertical direction. A fine-scale characterization of hydraulic
97 parameters is essential for the manageable and optimized utilization of subsurface reservoirs
98 through numerical modeling.

99 The feasibility and performance of DSS for reservoir formation deformation monitoring
100 have been shown in several recent field studies (Lei et al., 2019; Sun et al., 2019). Using a high-
101 resolution DSS tool, Zhang et al. (2019) and Zhang & Xue (2019) conducted laboratory tests to
102 demonstrate that quasi-static deformation field accompanying fluid injection and pore pressure
103 changes in reservoir rocks can be deployed to monitor fluid plume migration and gain information
104 on rock permeability and compressibility. More recently, Becker et al. (2020) reported successful
105 field experiments using DSS to monitor the displacement in fractured formation due to hydraulic
106 pressure stimulation.

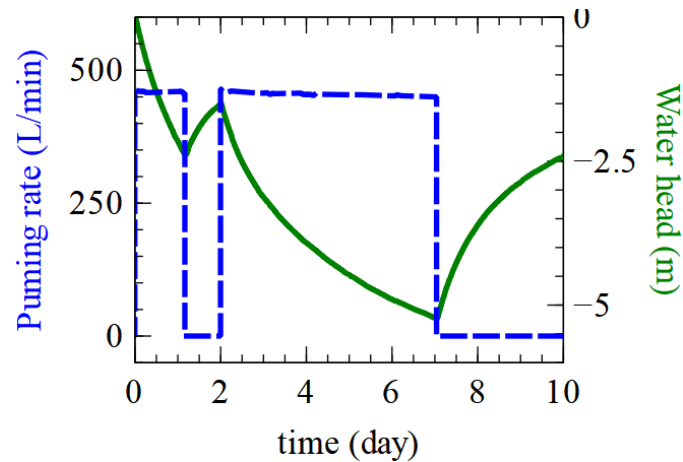
107 In this paper, we investigate the feasibility of using distributed strain data to estimate the
108 distributed hydraulic parameters with a coupled poroelastic model and a gradient-based inversion
109 algorithm. We first present a set of high-fidelity strain records from successful DSS application in
110 the monitoring of a field-scale aquifer pumping test. Then we provide the methods of the forward
111 and inverse modeling. Finally, we apply the methods to the synthetic and field studies and present
112 the one-dimensional meter-scale profiles of permeability and compressibility obtained using the
113 proposed inversion method. We also discussed the limitation of the method due to parameter
114 crosstalk and noise.

115 2. Aquifer pumping test with distributed strain sensing

116 2.1 Test site and operations

117 We conducted an aquifer pumping test in the rural area of Mobara City, Chiba, Japan.

118 Pressure drawdown-induced in situ formation deformation was monitored by a downhole-
119 installed high-resolution fiber optic DSS system. The target aquifer of the site was shallow at
120 approximately ~300 m deep. The aquifer had a simple hydrostratigraphic setting with alternation
121 strata of sandstone, mud and siltstone (Figure S1), which were formed in a shelf-margin delta
122 environment. In the past, the overexploitation of groundwater to extract dissolved natural gas and
123 iodine, agricultural irrigation, and other industrial utilizations have caused ground subsidence in
124 Chiba (Horiguchi, 1998). Since the 1970s, because of more severe regulations and reinjection,
125 subsidence has been largely mitigated. In this study, the water extraction depths (approximately
126 161–240 m) were fully perforated and belong to the Chonan Formation (Middle Pleistocene).
127 There is no evidence of existing fractures in the formation. In a previous study, Lei et al. (2019)
128 estimated the permeability of the entire formation to be approximately 470 mD. However,
129 permeability remains unclear for each depth. Aquifer water resources are frequently exploited
130 during spring and summer for agricultural irrigation. To avoid interference, the water pumping
131 test was performed in November. An existing agricultural well (Well1) was used for water
132 pumping. A monitoring well (Well2) equipped with optical fiber cables was located 175.1 m
133 away from the pumping well. Optical fiber cables were installed behind the well casing and
134 grouted in the cement annulus between the casing and aquifer formation. Another well (Well3)
135 located 5.5 m away from the monitoring well was perforated between depths of 186.8 and 193.6
136 m, which was used to monitor water head change.



137

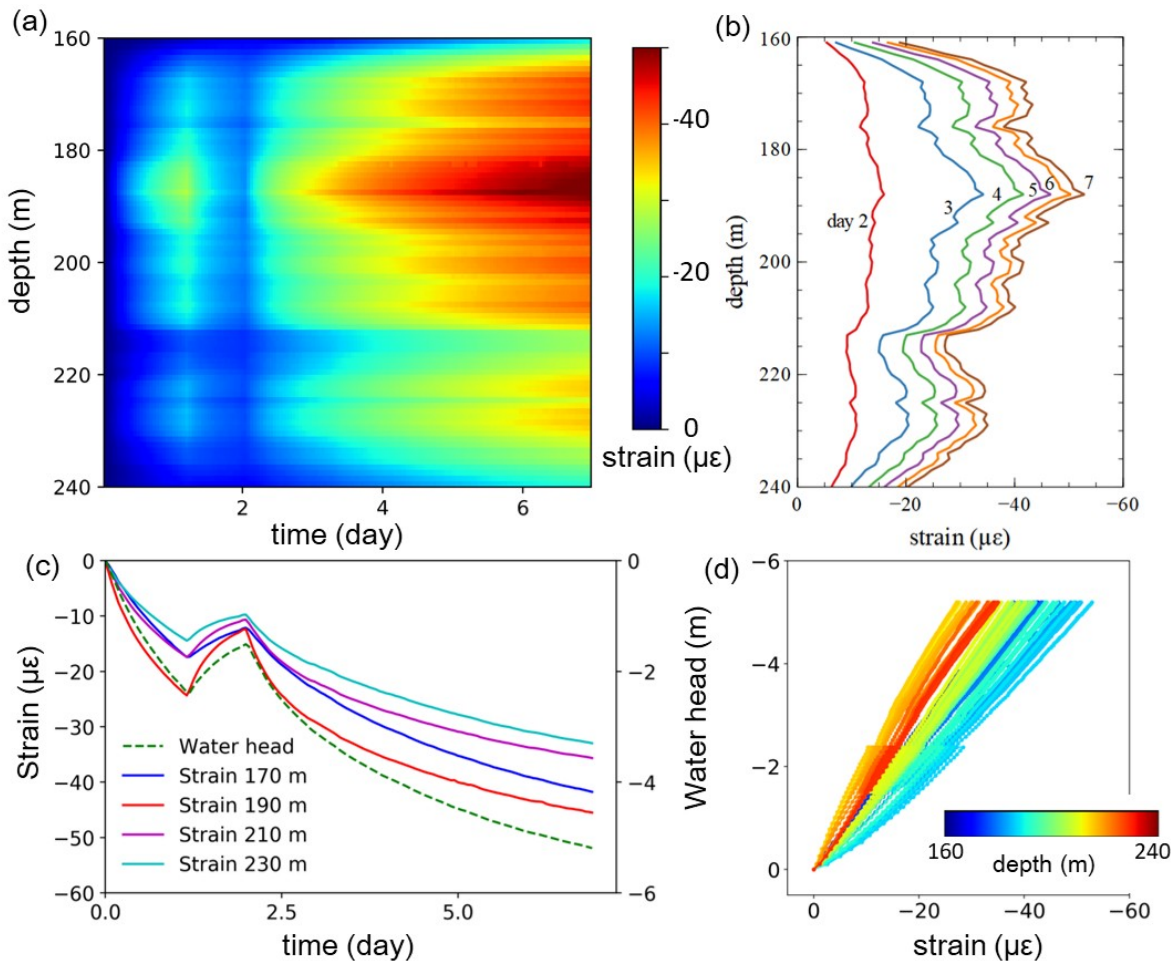
138 **Figure 1.** Recorded field data of water pumping rate and changes in water head.

139 Water extraction was conducted for approximately 7 days within the depth range of the
140 Chonan formation (Figure 1). There were two main pumping operation steps: (1) the initial
141 pumping (460 L/min) with the drawdown of the water head (lasting approximately 1.2 days),
142 which involved a temporary pause with the partial recovery of water head (approximately 0.8
143 days), and pumping (450 L/min) with the drawdown of water head (approximately 5 days), and
144 (2) the end of pumping and subsequent final recovery. In this study, we focused only on the
145 pumping stage. The fiber optic acquisition was performed using the Neubrescope NBX-8000
146 device and the Tunable Wavelength Coherent Optical Time Domain Reflectometry (TW-
147 COTDR) method (Kishida et al., 2014; Zhang et al., 2020). Continuous and distributed strain data
148 with an accuracy of $0.5 \mu\epsilon$, spatial resolution of 5 cm and a time resolution of approximately 1.1
149 hour was obtained during the entire pumping operation.

150 2.2 Distributed strain data

151 The distributed strain data obtained using DSS during the aquifer pumping test were
152 plotted as a time–depth–value image, depth–value profiles, and time–value trend curves (Figure
153 2a–c). In Figure 2, the spatiotemporal changes in strain responses during water extraction at the
154 well location with the installed optical fiber cable can be observed. The strain changes are
155 indicative of the impacted zones with aquifer pressure changes. The formation showed

156 compressive deformations during the water extraction stages due to a reduction in the pore fluid
157 pressure and effective stress, whereas it showed a temporal recovery (i.e., expansion deformation)
158 during the extraction pause between the first and second operation days. With continued water
159 extraction, the formation showed compressive deformations with gradually increasing
160 magnitudes. The largest compressive strain developed in the final stage and was approximately 50
161 $\mu\epsilon$, which is still considerably small. Along the vertical direction, variations in strain magnitude
162 appear in different depths, which may indicate depth-dependent heterogeneities in permeability
163 and compressibility. Particularly, large variations at several depths may indicate changes in the
164 lithological structure (sandstone-mudstone alternations). Two sections (from 160 to 212 m and
165 from 212 to 240 m) in the strain profile are distinguishable.



167 **Figure 2.** Vertical strain records at the observation well using distributed strain sensing during the
168 aquifer test by water extraction. The data are presented in the forms of (a) image, (b) depth
169 profiles, (c) time trends, and (d) cross plot with respect to water head. In (b), days 2 to 7
170 correspond to the x-axis of (a). In (d), only the depths between 170 and 230 m are plotted; linear
171 trends are shown.

172 Most of the strain data (at each depth) exhibit trends that are similar to the water head
173 (Figure 2c) with a nearly linear relationship (Figure 2d), which suggests linear poroelastic
174 deformation in the aquifer formation. The strain changes monitored by DSS are representative of
175 the deformation of aquifer formation due to a reduction in pressure. However, the depths near the
176 top and bottom boundaries show a nonlinear trend (Figure S2), which could be related to the
177 geomechanical effect. Most of the raw strain data (Figure S3) has smooth changes, which
178 suggests high quality data with a good signal/noise ratio; a few data points have error spikes
179 caused by incorrectly matching Rayleigh scattering power spectra using the cross-correlation
180 method. We used a median filter to remove these spikes when preparing the data for the
181 estimation of hydraulic parameters.

182 2.3 The benefits of DSS for reservoir geomechanics

183 The observations from DSS provide important constraints on the deformation in the
184 vertical direction and are complementary to surface-based observations (e.g., InSAR), which have
185 been used to monitor fluid migration and estimate lateral permeability distribution at large scales
186 (Bohloli et al., 2018; Jha et al., 2015; Vasco et al., 2008). As shown by the data, even a small
187 induced strain ($\sim 1 \mu\epsilon$) in the aquifer formation can be detected. This indicates that DSS should be
188 useful for more detailed geomechanical studies, such as for tracking, evaluating, and managing
189 aquifer deformation and understanding the role of underground deformation to surface
190 subsidence. For instance, the extent of aquifer deformation due to seasonal massive agricultural
191 irrigation can be evaluated in situ and in real time. The contribution of formation heterogeneity of

192 each interval to total surface displacement and the mainly deforming parts can be understood by
193 examining the local strain. Whether the aquifer has recovered to a normal state can be determined
194 by checking the strain changes, by which the proper management of ground water resources is
195 possible (Gleeson et al., 2012). Similar functionality could be utilized for CO₂ or natural gas
196 storage in underground reservoirs. The real-time DSS data can offer accurate information to
197 understand geomechanical deformation state as well as to evaluate geomechanical risk; it is also
198 useful for tracking pressure and plume migrations (Zhang et al., 2019; Zhang & Xue, 2019;
199 Murdoch et al., 2020).

200 **3 From strain to hydraulic parameters: forward and inverse models**

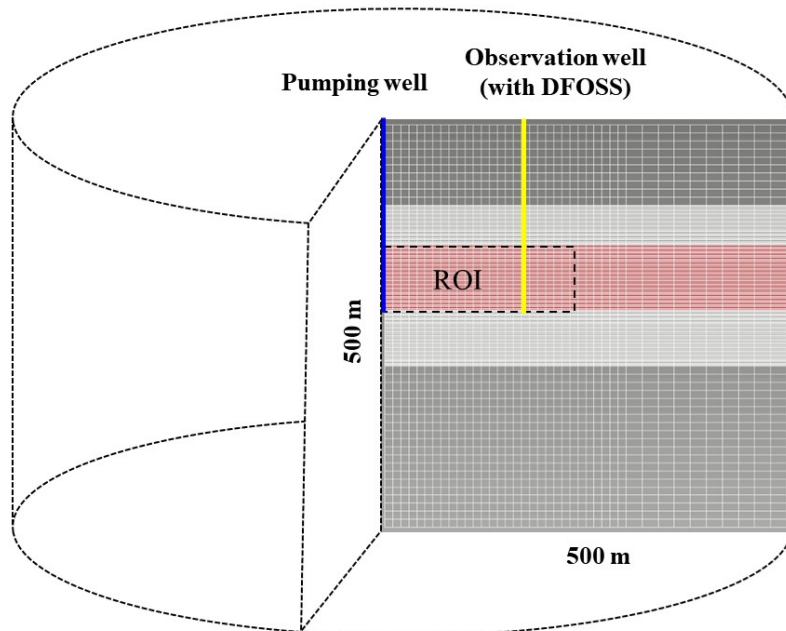
201 Beyond the above direct application of DSS related to geomechanical phenomena, the
202 induced poroelastic deformation by formation pressure change may carry the information of
203 hydraulic parameters. According to Biot's poroelastic theory, the hydromechanical coupling
204 problems can be categorized as solid-to-fluid and fluid-to-solid (Wang, 2017). For example,
205 consolidation induced excess fluid pressure and earthquake-driven fluid migration are solid-to-
206 fluid coupling. Alternatively, fluid-to-solid coupling is usually used to describe changes in fluid
207 pressure (due to injection or extraction) modifying the effective stress and deforming the rock. In
208 the latter coupling, permeability and compressibility together control the evolution of pressure
209 and strain. Inversely, by monitoring the strain changes of an aquifer, the fluid-to-solid coupling
210 may provide an opportunity to characterize the two hydraulic parameters.

211 3.1 Forward model for poroelastic strain calculation

212 We employed a coupled hydromechanical model based on the poroelastic theory (Biot,
213 1941) to calculate strain due to hydraulic activities, e.g., aquifer pumping test. The main equations
214 refer to those classic literatures (Biot, 1941; Cheng, 2016; Rice & Cleary, 1976; Wang, 2017).
215 Through the forward problem solving the coupled hydromechanical equations with setting

216 hydraulic and mechanical parameters, the spatial changes in stress, strain and pore pressure of the
217 formation induced by water pumping can be calculated.

218 We constructed an axisymmetric cylinder two-dimensional model with Cartesian
219 geometry (Figure 3), with the vertical axis representing the location of the pumping well to
220 approximate the aquifer setting. To avoid possible impacts of boundary effects on strain changes
221 in the testing region, which is the region of interest (ROI), we set a much larger modeling domain
222 (500×500 m) than the ROI size (200×100 m) and set the boundary remote from the ROI. We
223 used dense Cartesian mesh gridding (10×1 m) within the ROI and nearby regions and sparse
224 gridding in outside regions. There were total 9,200 elements and approximately 28,000 of degree
225 of freedom in the model. The injection section was between 161 and 240 m (80 m thick). The
226 normal component of the displacements at the outer side and bottom of the model was set to 0. A
227 Dirichlet constant pore pressure condition was set at the outer side. The water extraction source
228 condition was set at the well boundary with time-dependent flux. The forward model starts from
229 an initial hydrostatic equilibrium state; only the latter changes in pore pressure, stress and strain
230 caused by water pumping were considered.



232 **Figure 3.** Schematic of the forward model.

233 In the hydromechanical model, we set one-dimensional layered variations (with a length
234 interval of 1 m) of permeability (k) and compressibility (C_α), which are considered as the
235 reciprocal of bulk modulus, within the ROI along the vertical direction. Following Lei et al.,
236 (2019), we applied uniform porosity ($\phi = 0.43$), Biot's coefficient ($\alpha = 1$), water compressibility ($C_f = 4.5 \times 10^{-10}$ 1/Pa), and Poisson's ratio ($\nu = 0.29$) for all modeling. Only isotropic permeability
237 and compressibility were considered. An observation well was located 175.1 m away from the
238 pumping well. The same pumping rate in the field study was set. In this study, we only consider
239 the vertical strain component, which is related to the DSS measurement. We have limited our
240 study to the small and linear poroelastic deformation mechanism. We applied the open source
241 finite element modeling framework MOOSE to solve the forward poroelastic model (Wilkins et
242 al., 2020).

244 3.2 Inverse models for hydraulic parameter estimation from strain

245 The inverse problem is formulated by minimizing the objective function $f(x)$ accounting
246 for the difference between the measured and modeled strain values:

$$247 \quad \text{minimize } f(x) = \sum_{i=1}^n \dot{\epsilon}_i \epsilon_i(x) - \bar{\epsilon}_i(x) \dot{\epsilon}_i \quad (1)$$

248 where $\bar{\epsilon}_i$ and ϵ_i represent the measured and modeled strain values, respectively. There is a total of
249 $n = 80 \times 2$ unknowns (x) of permeability and compressibility for each layer (1 m thick) within the
250 80 m thickness formation. We provided an initial guess values (10 mD for the permeability and
251 1×10^{-9} 1/Pa for the compressibility) and bound constraints for the parameter ranges.

253 We used a nonlinear least-squares method with the trust region reflective algorithm
254 (Branch et al., 1999) to solve the minimization problem (Virtanen et al., 2020). In the algorithm,
255 the subset of the region of the nonlinear objective function (referred to as the trust region) can be

256 approximated using a quadratic model function. The algorithm iteratively solves subspace
257 problems in trust regions by the approximate Gauss–Newton method, with trust region shape and
258 size determined by the distance from the bounds and the gradient direction. The algorithm
259 considers search directions reflected from the bounds using a reflective transformation technique
260 to improve convergence for problems with bound constraints; moreover it can properly handle
261 bound constraints for large-scale nonlinear least-squares problems. For the method, it is necessary
262 to calculate the objective function gradient (i.e. Jacobian matrix) and the Hessian matrix
263 approximation. For the significant spatial heterogeneity and coupling nature in the model, the
264 forward modeling by a single CPU is slow (~10 min). Accordingly, we used a supercomputer
265 system (Oakbridge-CX Supercomputer System, University of Tokyo) to accelerate the Jacobian
266 computation in parallel. We also used the Tikhonov regularization technique to condition the
267 problem (e.g. by minimizing the sum of parameter gradient) and stabilize the estimation.

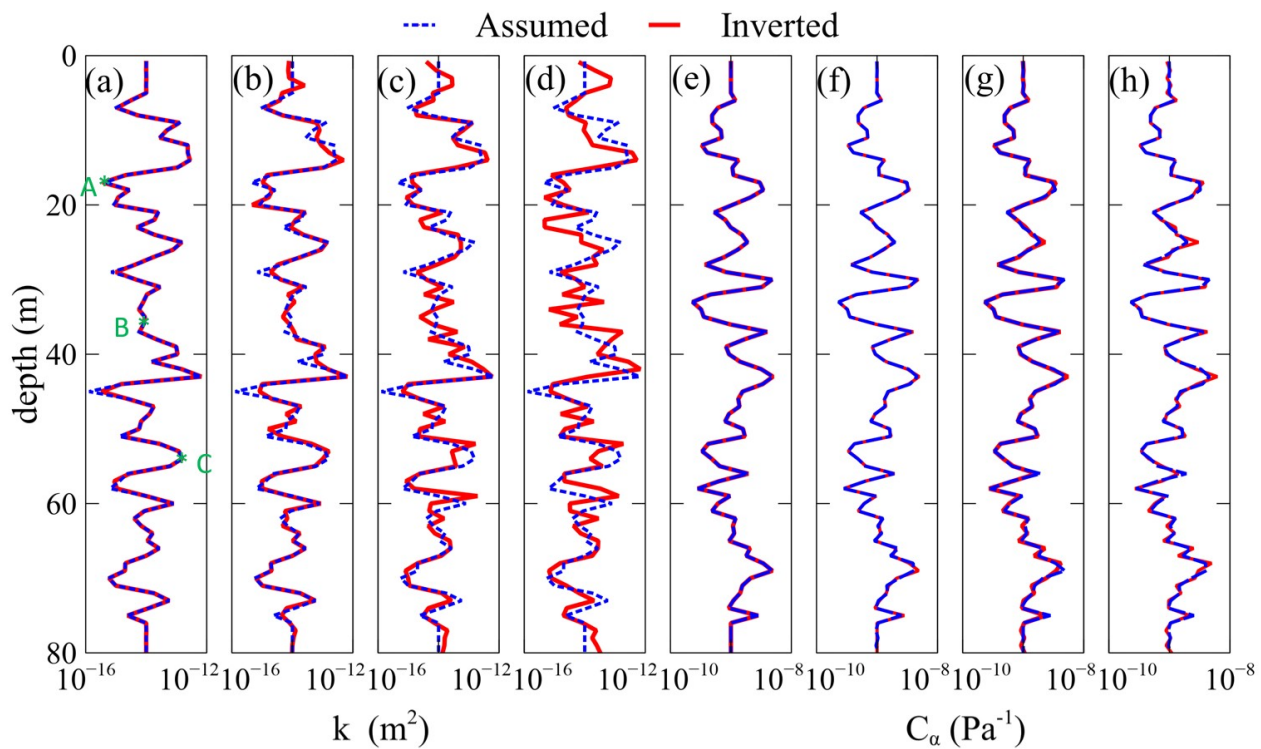
268 In principle, the inversion of hydraulic parameters using distributed strain data is similar
269 to those used in the inversion of flow rate and permeability using distributed temperature sensing
270 data (Becker et al., 2004; Maldaner et al., 2019; Medina et al., 2020). However, there are some
271 inherent difficulties in the current inverse problem. The unknown parameters, permeability and
272 compressibility, both influence the strain. They may have different sensitivities and numerical
273 ranges that affect the strain changes; they may also have the parameter crosstalk (or trade-off)
274 problem (Aster et al., 2018; Menke, 2018).

275 **4 Hydraulic parameter estimation**

276 4.1 Synthetic tests

277 We conducted numerical synthetic studies both with and without noise to examine the
278 feasibility of the proposed method for inversely estimating hydraulic parameters using distributed
279 strain data. In the synthetic model, the settings were the same as the latter modeling for the field

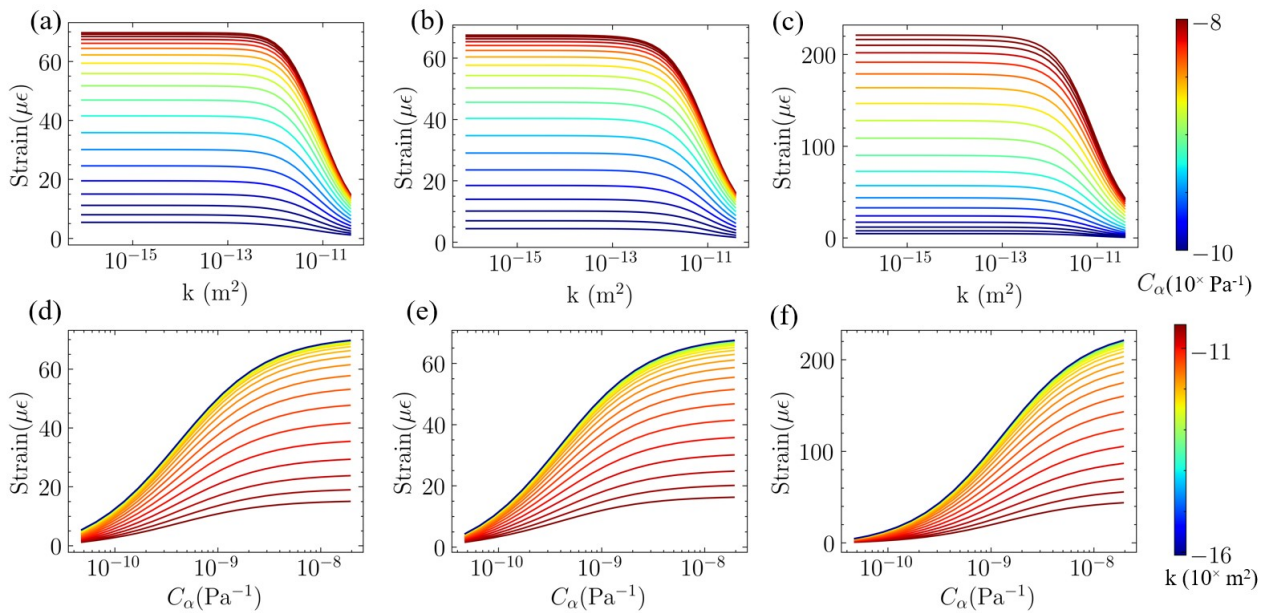
280 study, but we set the synthetic model with assumed permeability and compressibility values
281 (Figure 4a–b). By running the forward modeling once, we obtained synthetic transient strain
282 records at each depth of the virtual observation well. For the case with noise, we added Gaussian
283 random noise with a standard deviation (σ) of 0.5 (which corresponds to the measurement
284 accuracy of the DSS tool in the field test), 2 and 5 $\mu\epsilon$ (approximately 10% of the average strain
285 for the record at the zone with lowest strain). Permeability and compressibility were then set in
286 the formation as unknowns and estimated inversely by reducing the difference between the
287 modeled and synthetic strain data. The assumed permeability and compressibility were given
288 arbitrarily. To generate abundant variations, a Gaussian correlation distribution model with a
289 correlation length of 1 m was used. Uncorrelated distributions were realized for the permeability
290 and compressibility fields. The distributions included some sharp spikes (e.g. 1 m), which were
291 used to understand the spatial resolution of the inverse model.



293 **Figure 4.** (a–d) Inversely estimated permeability and (e–h) compressibility profiles compared
 294 with the assumed true model parameters in the synthetic model. In the estimation of (a) and (e),
 295 the synthetic strain data without noise was used; for (b) and (f), (c) and (g), and (d) and (h), the
 296 synthetic strain data were used with added Gaussian random noise and standard deviations of 0.5,
 297 2, and 5 $\mu\epsilon$, respectively.

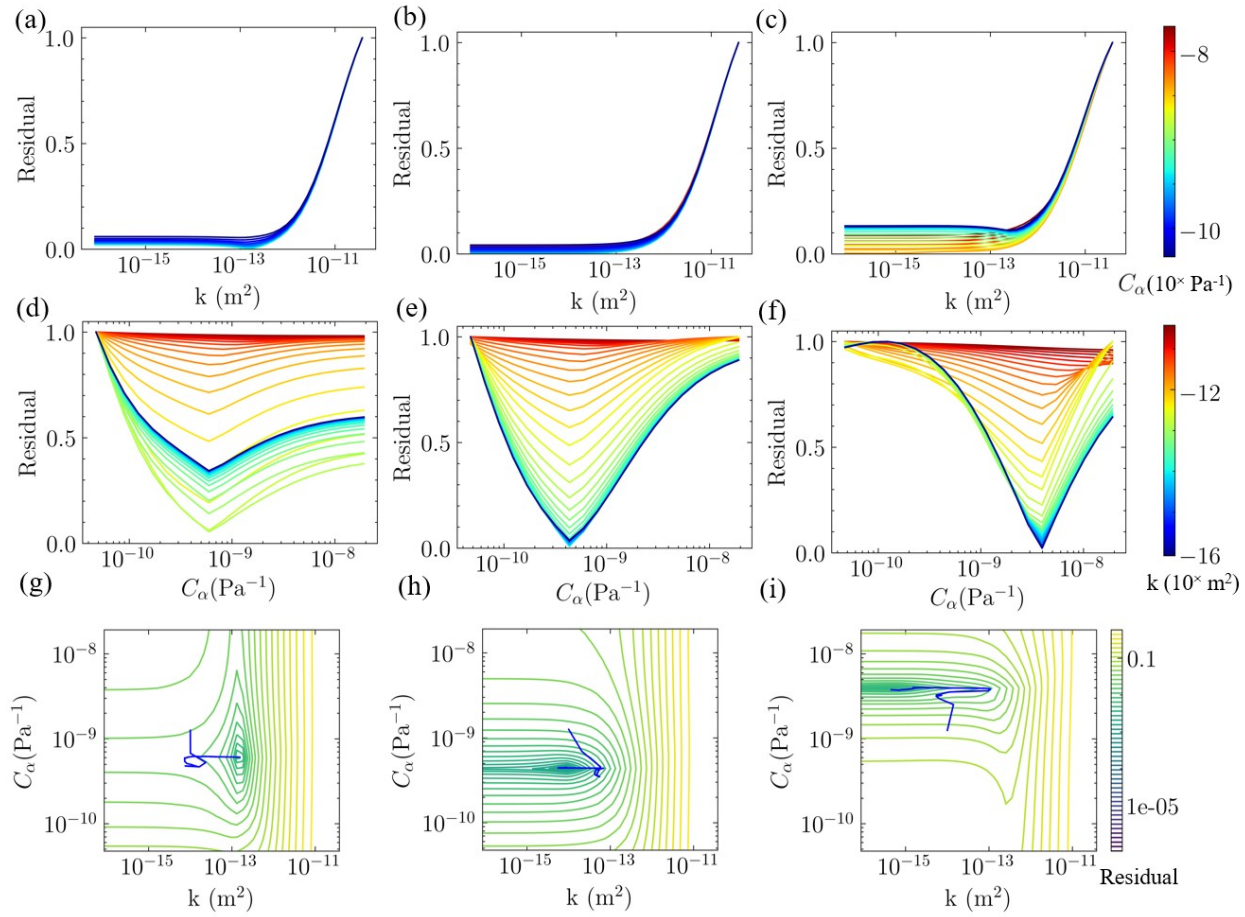
298

299

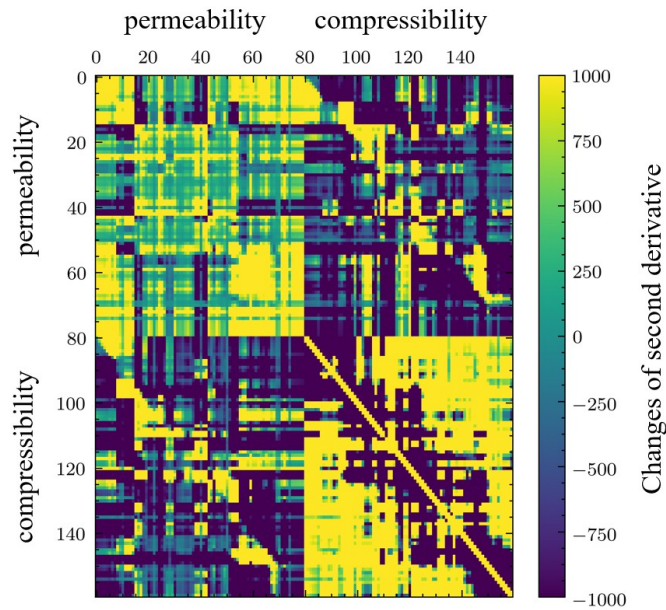


300

301 **Figure 5.** (a-c) Strain change with respect to permeability and (d-f) compressibility for locations
302 A, B and C in Figure 4a.



306 **Figure 6.** Normalized sensitivity of the residual of the objective function with respect to (a-c)
307 permeability, (d-f) compressibility, and (g-i) the process of finding the best solution in the solution
308 space for locations A, B and C in Figure 4a.

309
310

311 **Figure 7.** Approximate Hessian matrix of the objective function near the optimal solution of the
312 synthetic study.

313

314 The sensitivities of changes in strain and the objective function (expressed by the residual
315 between assumed and calculated strains) with respect to permeability and compressibility at
316 several locations (Figure 4) were investigated (Figures 5 and 6 and Figure S4). The local strain
317 change generally shows a reducing trend with an increase in permeability and an increasing trend
318 to with an increase in compressibility. The strain sensitivity has a significant change in the higher
319 permeability range, e.g. $> 10^{-13} \text{ m}^2$, whereas it shows only slight variations in the lower
320 permeability range. In contrast, the local strain shows more gradual changes in the entire range of
321 $10^{-10} - 10^{-8} \text{ Pa}^{-1}$. The changes in strain magnitude are different and they depend on the spatial
322 combination of the heterogeneity in permeability and compressibility. For example, for the points

323 A and B (Figure 4a), the largest strain is smaller than $70 \mu\epsilon$, whereas, for point C, the strain
324 reaches approximately $210 \mu\epsilon$ (Figure S4). However, after normalization by the maximum strain
325 change, these points show similar trends (Figure S4a–f).

326 Next, we identify the global minimum of the objective function in the parameter ranges
327 (Figure 6a–i). Corresponding to the strain sensitivity, in the solution space with higher
328 permeability in the range, the path of residual reduction to the global minimum is more distinct.
329 However, the residual has only slight changes in the range where the permeability is not high, e.g.
330 $< 10^{-13} \text{ m}^2$ (Figure 6a). The global minimum is less visible in the range. By contrast, the residual
331 has obvious changes in the entire range of 10^{-10} – 10^{-8} Pa^{-1} in the space of compressibility for the
332 permeability of $< 10^{-12} \text{ m}^2$ and the global minimum is also easily identifiable. Overall, Figures 5
333 and 6 indicate that the minimum for permeability is not stable with respect to the addition of
334 errors when $k < 10^{-13} \text{ m}^2$. For sensitivity changes, it should be more difficult to estimate
335 permeability for layers with low permeability values.

336 When simultaneously estimating both permeability and compressibility, one concern is
337 that the parameter crosstalk problem may affect the iterative process in finding the true optimal
338 solution. We can observe large changes in the off-diagonal values in the permeability or
339 compressibility block and the crosstalk blocks in the calculated approximate Hessian matrix
340 (Figure 7). Because the two types of unknown parameters both influence the strain, permeability
341 and compressibility both affect each other. Moreover, the effect can propagate from one location
342 to another. Because the total water pumping rate is constrained, in the modeling, a change in the
343 permeability of a location will not only change the local flow rate but also the flow rate at other
344 locations, which affects the parameter estimation.

345 Despite these difficulties, an optimal solution for simultaneously estimating both
346 permeability and compressibility can be obtained through inverse modeling insofar as strain data

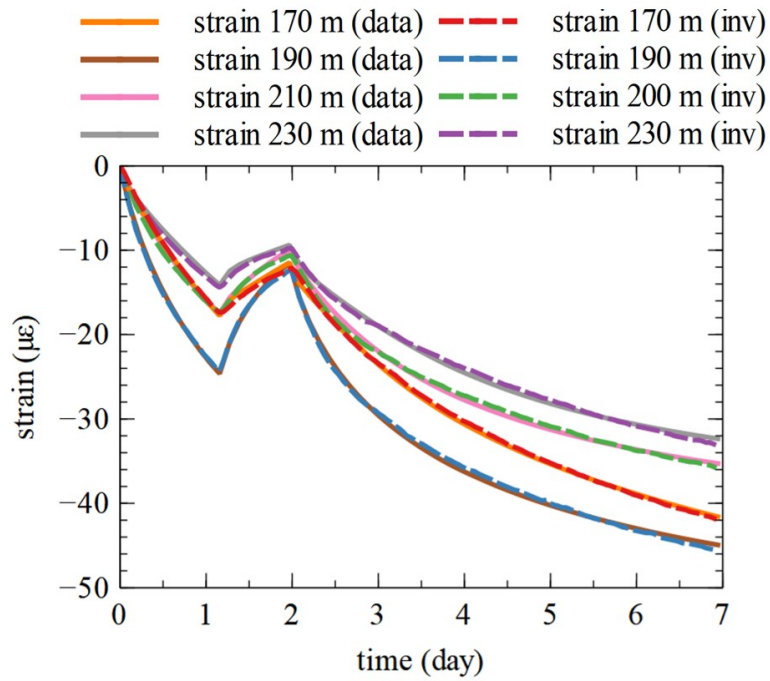
347 are free from noise. Figure 4a and e show the final best estimated compressibility and
348 permeability with the assumed distribution. Most parts of the permeability structure are recovered
349 except some local parts with small values, whereas the inversely estimated compressibility almost
350 overlaps the assumed distribution. Particularly, because of the spatially dense coverage of strain
351 records, even the values for very narrow spikes can be correctly estimated. The results show that
352 the majority permeability and compressibility structures can be inversely estimated with errors of
353 $<2\%$. The errors in low-permeability parts can be understood from the low sensitivity of the
354 permeability values to the objective function (see Figure 6a–c), which makes it difficult for the
355 gradient-based optimization algorithm to find the global minimum. Figure 6g–i shows the
356 iterative process for finding the best solution.

357 By contrast, if the strain data contain noise (e.g. $\sigma = 0.5 \mu\epsilon$, in Figure 4b and f), it is
358 difficult to obtain the global optimal solution at some locations using the current gradient-based
359 algorithm (Figure 4c and d). Because of the integrated effect of parameter crosstalk and noise, the
360 solution may be entrapped into some local minimums near the global solution and cannot further
361 reach the residual corresponding to the global solution. The influence becomes more severe when
362 the noise level increases (e.g. 2 and 5 $\mu\epsilon$ in Figure 4e and f). This has a large impact on the
363 permeability estimation as indicated by the distinct sensitivity changes in Figures 5 and 6. The
364 minimum in the objective function may be not stable with respect to errors if the noise level is
365 high (Figure 6). The influence is non-local and can propagate into other locations because of the
366 constraint of the total flow rate. Regardless, overall, the magnitude and main structure of
367 hydraulic parameters can be largely estimated. The results of synthetic studies demonstrate the
368 feasibility of the proposed method with low noise. The low noise level can be guaranteed by high
369 accuracy (0.5 $\mu\epsilon$) and stability in the field measurement using DSS.

370 4.2 Inversion results of the field study

371 Next, we inversely estimated the formation permeability and compressibility for the field
372 study. In the field model, all settings (domain, boundary conditions, elastic and fluid flow
373 properties) were the same as the synthetic model, but we used the true observations of strain
374 recorded by DSS. To reduce the computational dimension, we upscaled the measured strain data
375 from 5 cm intervals to 1 m length by arithmetic average. The entire 80 m-thick formation was
376 divided into 80 layers with 80 series of strain records and 80×2 unknowns of permeability and
377 compressibility in the inversion model.

378 The parameter sensitivity shows similar characteristics to the synthetic study (Figure S6a–
379 i). Similar to the synthetic study with noise, it is difficult to obtain a unique global solution by
380 reducing the residual by the gradient-based algorithm. Instead, multiple near-optimal local
381 solutions with similar levels of residuals exist. Moreover, because of the parameter crosstalk
382 problem, the local solutions may be very distinct in the values of hydraulic parameters. In our
383 tests, the inverted permeability of local solutions can have a difference of two orders of
384 magnitude. In all these solutions, the modeled strain changes seem well consistent with the
385 measurements (Figure 8). We selected one preferred solution with the information of the water
386 head change in Well3 (Figure S5). The preferred solution has a good correspondence between the
387 modelled and measured aquifer water head change (Figure S8). This implies that the additional
388 head constraint could be helpful in mitigating the trade-off between permeability and
389 compressibility in the inversion. The solutions in the solving space of three points (Figure 9a) are
390 shown in Figure S6g–i.



391

392 **Figure 8.** Modeled strain changes at several selected depths (170, 190, 210, and 230 m) of the
 393 best solution from inverse estimation compared with the field-measured strain data using DSS.

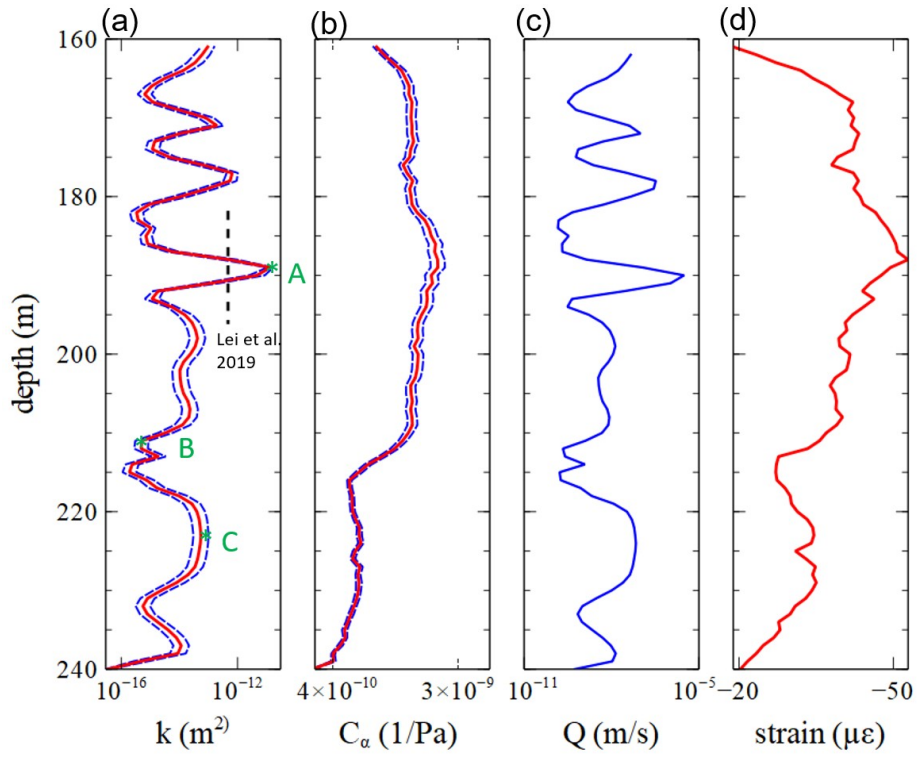
394

395 The inversely estimated permeability and compressibility (k and C_a) profiles are shown in
 396 Figure 9a and 9b. The estimated permeability ranges from approximately 0.1 mD to 1 D in
 397 different parts of the profile. There are several groups with higher permeability (>20 mD). The
 398 intervals with high and low permeability (near 190 and 215 m, respectively) are consistent with
 399 the strain peak and trough as shown in Figure 9d. Although there are some inconsistent parts, the
 400 depth intervals with higher permeability values generally point to layers that mainly comprise
 401 sandstones, as shown by the Electrical Micro Imaging (EMI) in Figure 10f. It seems that some of
 402 the low permeability intervals can be also matched to some featured spikes in the well logs (V_p ,
 403 V_s and gamma ray) in Figure 10c–e. The estimated flow rate (Figure 9c) shows a similar shape to
 404 the permeability profile. The lithological changes and permeability structure determine the spatial
 405 migration of water as well as the propagation and distribution of pore fluid pressure, which
 406 further controls the formation deformation as described by poroelastic theory.

407 The permeability range is largely consistent with the estimated single permeability value
408 (470 mD; Figure 9a) which is based on the data of hydraulic head changes for the entire formation
409 of a previous study (Lei et al., 2019). Some inconsistent parts between the estimated permeability
410 structure and EMI can be attributed to the fact that, physically, the lithological changes may only
411 partially reflect the permeability structure. For example, there may be invisible micro-fractures
412 that increase permeability.

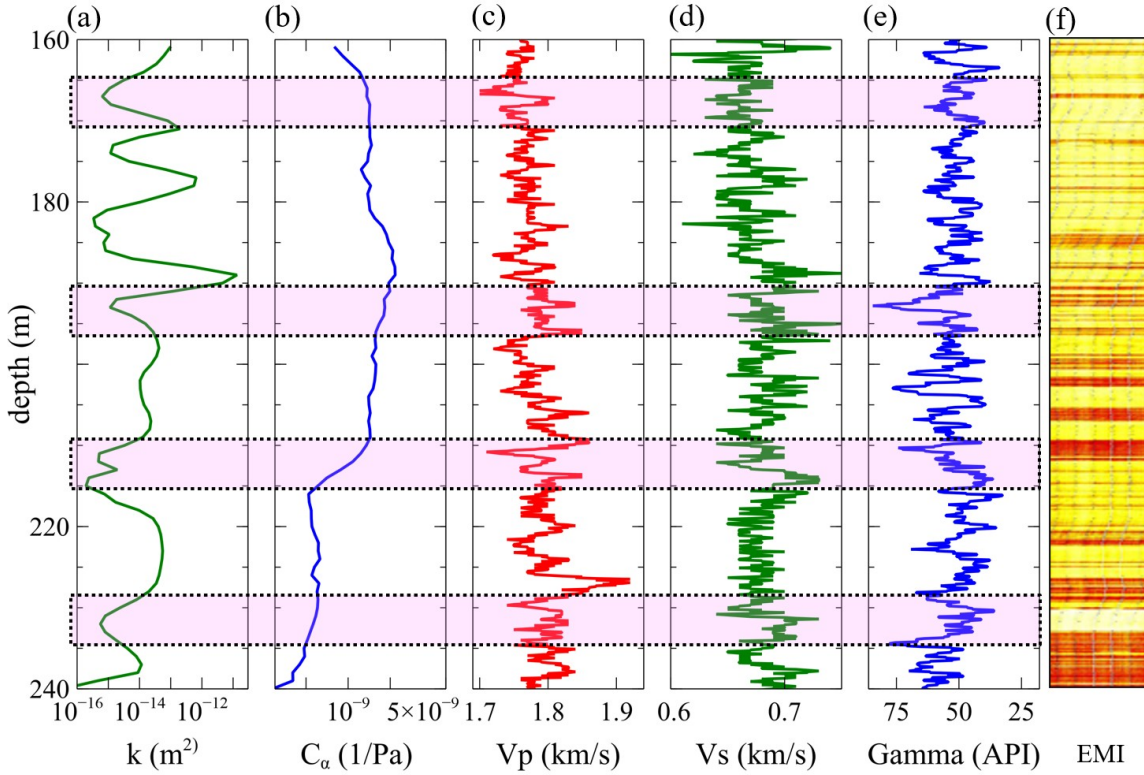
413 The estimated compressibility generally shows a pattern similar to the spatial strain
414 distribution; however, the changes are subtler. The compressibility varies between 3.6×10^{-10} and
415 2.8×10^{-9} 1/Pa along the profile. As strain changes, two parts (from 160 to 215 m and from 215 to
416 240 m) in the compressibility profile can be distinguished. It seems that the corresponding
417 changes are also distinguishable from the Vp and Vs well logs.

418 Overall, the permeability and compressibility determine the strain pattern. Some local
419 strain fluctuations (e.g. peaks or troughs) are predominated by the permeability structure. For a
420 multi-layer formation, the overall changes in the aquifer pressure and deformation are partitioned
421 to the sub-layers. Layers with high permeability and compressibility can easily develop greater
422 deformation and thus dominate the deformation pattern. Hydromechanically, the lithological
423 layers may be grouped into several units. The inversely estimated hydraulic parameters can be
424 generally and reasonably interpreted from the geological information.



425

426 **Figure 9.** The inversely estimated profiles of (a) permeability, (b) compressibility and (c) flow
427 rate (the Darcy velocity) with (d) the strain profile in the final. The dashed lines in (a) and (b)
428 indicate the uncertainty of one standard deviation in the estimation obtained from the
429 approximation of the Hessian matrix.



430
431 **Figure 10.** The inversely estimated profiles of (a) permeability and (b) compressibility, with well
432 logs of (c) compressive wave velocity, (d) shear wave velocity, (e) gamma ray, and (f) EMI of the
433 well showing the lithological structure (sandstone–mudstone alternations).

434

435 **5. Discussions and conclusions**

436 In conventional studies, one primary issue causing difficulty in obtaining hydraulic
437 parameters is the measurement of either in situ formation pressure or hydraulic head for
438 multilayer formation. It is not practical to measure the hydraulic head at each depth location of
439 each layer in a well (or in many wells) when the formation develops many layers, such as the

440 sandstone–mud alternations in this study. The measurement of in situ formation pressure also has
441 an intrinsic problem in that it is not feasible to embed many discrete pressure sensors in the
442 formation along a wellbore.

443 Unlike conventional pressure sensors, as shown by this study, an optical fiber cable placed
444 in the cement between the well casing and the sedimentary formation can be deployed for the
445 distributed sensing of hydromechanical responses with high fidelity measurements. Although the
446 measured parameter is strain and not pressure, under the linear poroelastic deformation
447 mechanism (Biot, 1941; Cheng, 2016; Rice & Cleary, 1976; Wang, 2017), the pore pressure
448 induced strain change is closely associated with changes in pore pressure (Berg et al., 2015;
449 Burbey, 2001; Hesse & Stadler, 2014).

450 As demonstrated in this study, strain data can provide a similar function to pore pressure.
451 The recorded strain data clearly show the spatial distribution and migration of pore pressure
452 perturbations. Parameter estimation using DSS data can provide additional benefits with detailed
453 information of formation properties in the vertical direction that are beyond previously mentioned
454 geomechanical applications. The information should be useful for understanding the contribution
455 of each layer to the overall fluid transport and pressure evolution (Figure 9c and d), as well as for
456 determining appropriate fluid injection or extraction strategy (such as interval and rate) in
457 underground fluid storage (e.g., CO₂ storage) projects. The responses at the initial stages can be
458 used to characterize reservoir permeability and compressibility structure, which could assist in
459 continued injection design and pressure management to avoid potential geomechanical risks
460 (Buscheck et al., 2012).

461 One of the limitations of the proposed method is concerned with the estimation of layers
462 with low-permeability values. This can be attributed to the low sensitivity of strain changes for a
463 permeability $< 10^{-13}$ m². Particularly, when a larger measurement noise ($\sigma = 5 \mu\epsilon$) is added in the

464 synthetic study, it is difficult to further reduce the residual of the objective function and obtain the
465 global solution, and the estimation of permeability becomes unstable using the current gradient-
466 based minimization method. In the field case, the errors coming from upscaling using the
467 arithmetic averaging method may also affect the parameter estimation. Because of the combined
468 effect of parameter crosstalk and data noise, the current solution may be solely a near-optimal
469 solution. A choice of other inversion methods (such as the adjoint-based method; Vasco and Mail,
470 2020) and global optimization methods (Comola et al., 2016; Jones, et al., 1998), or a better
471 regularization technique (Aster et al., 2018; Menke, 2018; Ren & Kalscheuer, 2020) may improve
472 the solution.

473 Additionally, some unconsidered physical mechanisms may also affect the modelling.
474 These may include the pressure or strain dependent permeability relationship, small inelastic
475 contribution, depth dependent Biot's coefficient, anisotropy in the properties, and neglected
476 changes in Poisson's ratio. Because there is no constraint of lateral strain, we only used one
477 constant value for Poisson's ratio. A future survey with measurements of lateral strain (e.g. by a
478 helical installation of the fiber cable) may be helpful for improved estimation.

479 In this study, for the experimental design and available data, we have attempted to
480 simultaneously estimate both permeability and compressibility. The simultaneous estimation of
481 two parameters significantly increases the inversion difficulty compared with estimating one
482 parameter. In practice, the compressibility can be constrained first by an improved testing
483 strategy. For example, two or more steady-state steps resulting from constant head testing can be
484 used to analytically calculate compressibility, making the estimation of permeability less
485 challenging. By constant head testing, the constraint from the total flow rate can be removed, and
486 thus, the inverse modeling can be made effortless.

487 Furthermore, we approximated the aquifer as a one-dimensional layered property model
488 (but with an axisymmetric two-dimensional model) and neglected lateral changes for simplicity.
489 The approximation may result in model errors. A cross-well hydraulic tomography (Rucci et al.,
490 2010; Vasco et al., 2014), using the information of onset time, amplitude or phase changes in
491 strain signals, may be helpful for resolving two-dimensional variations, as well as for reducing
492 modeling errors and extending the method to more complex aquifers. The use of DSS makes
493 cross-well tests easier to conduct; it also makes it easier to view time-lapse changes between tests.

494 The high-quality DSS data acquired in the field study and the good correspondence
495 between strain and formation pressure suggest that the recorded strain can be attributed to
496 formation deformation. One concern is that it is unclear whether the measured strain is partially or
497 fully representative of the formation deformation. Some studies have considered the strain
498 transfer problem for unconsolidated formation with loose coupling between formation and cement
499 (Zhang et al., 2020). However, according to Becker et al. (2018), for a stiff rock formation with
500 good coupling between formation and cement (without slippage), the strain measurement by DSS
501 represents formation deformation.

502 Another concern is related to the effect of parameter correlation between permeability and
503 compressibility in the simultaneous estimation. The parameter correlation could lead to problems
504 in hydraulic tomographic studies because the data used to estimate spatial parameters in the
505 underdetermined problems were limited. However, in our study, we find that the estimations are
506 unaffected when intentionally setting correlated or uncorrelated permeability and compressibility
507 fields in synthetic testing. In our method, we calculated parameters with the strong constraint
508 from the measurement of each individual layer. The permeability and compressibility of each
509 layer are mostly constrained by the strain changes in each layer. Within each layer, the response is
510 similar to that of conventional well testing with an assumption of uniform properties between

511 wells; however, the response is still influenced by neighboring layers and the constraint from the
512 total flow rate.

513

514 **Acknowledgments**

515

516 We thank Dr. D. Vasco, three anomalous reviewers, and the associate editor for their critical
517 comments and suggestions towards improving the manuscript. This paper is based on results
518 obtained from a project (JPNP18006) commissioned by the New Energy and Industrial
519 Technology Development Organization (NEDO) and the Ministry of Economy, Trade and
520 Industry (METI) of Japan. This research is partially supported by Initiative on Promotion of
521 Supercomputing for Young or Women Researchers, Supercomputing Division, Information
522 Technology Center, The University of Tokyo (for the usage of supercomputer system).

523

524 **Data Availability Statement**

525 The strain data are available at <http://dx.doi.org/10.6084/m9.figshare.12178656>.

526

527 **References**

528 Alghamdi, A., Hesse, M. A., Chen, J., & Ghattas, O. (2020). Bayesian Poroelastic Aquifer

529 Characterization From InSAR Surface Deformation Data. Part I: Maximum A Posteriori

530 Estimate. *Water Resources Research*, 56(10), e2020WR027391.

531 <https://doi.org/https://doi.org/10.1029/2020WR027391>

532 Anderson, M. P., Woessner, W. W., & Hunt, R. J. (2015). *Applied groundwater modeling:*

533 *simulation of flow and advective transport*. Academic press.

534 Aster, R. C., Borchers, B., & Thurber, C. H. (2018). *Parameter estimation and inverse problems*.

Elsevier.

- 536 Bear, J., & Verruijt, A. (2012). *Modeling groundwater flow and pollution* (Vol. 2). Springer
537 Science & Business Media.
- 538 Becker, M W, Georgian, T., Ambrose, H., Siniscalchi, J., & Fredrick, K. (2004). Estimating flow
539 and flux of ground water discharge using water temperature and velocity. *Journal of*
540 *Hydrology*, 296(1), 221–233. [https://doi.org/https://doi.org/10.1016/j.jhydrol.2004.03.025](https://doi.org/10.1016/j.jhydrol.2004.03.025)
- 541 Becker, M W, Coleman, T. I., & Ciervo, C. C. (2020). Distributed Acoustic Sensing (DAS) as a
542 Distributed Hydraulic Sensor in Fractured Bedrock. *Water Resources Research*,
543 e2020WR028140.
- 544 Becker, M W, Ciervo, C., & Coleman, T. (2018). A Slimhole Approach to Measuring Distributed
545 Hydromechanical Strain in Fractured Geothermal Reservoirs. In *Proceedings of the 43rd*
546 *Workshop on Geothermal Reservoir Engineering Stanford University, Palo Alto, CA, USA*
547 (pp. 12–14).
- 548 Bohlooli, B., Bjørnarå, T. I., Park, J., & Rucci, A. (2018). Can we use surface uplift data for
549 reservoir performance monitoring? A case study from In Salah, Algeria. *International*
550 *Journal of Greenhouse Gas Control*, 76(June 2017), 200–207.
551 <https://doi.org/10.1016/j.ijggc.2018.06.024>
- 552 Branch, M. A., Coleman, T. F., & Li, Y. (1999). A subspace, interior, and conjugate gradient
553 method for large-scale bound-constrained minimization problems. *SIAM Journal on*
554 *Scientific Computing*, 21(1), 1–23.
- 555 Buscheck, T. A., Sun, Y., Chen, M., Hao, Y., Wolery, T. J., Bourcier, W. L., et al. (2012). Active
556 CO2 reservoir management for carbon storage: Analysis of operational strategies to relieve
557 pressure buildup and improve injectivity. *International Journal of Greenhouse Gas Control*,
558 6, 230–245.
- 559 Commer, M., Pride, S. R., Vasco, D. W., Finsterle, S., & Kowalsky, M. B. (2020). Imaging of a

560 fluid injection process using geophysical data—A didactic example. *Geophysics*, 85(2), W1–
561 W16.

562 Comola, F., Janna, C., Lovison, A., Minini, M., Tamburini, A., & Teatini, P. (2016). Efficient
563 global optimization of reservoir geomechanical parameters based on synthetic aperture
564 radar-derived ground displacements. *Geophysics*, 81(3), M23–M33. [https://doi.org/10.1190/
565 GEO2015-0402.1](https://doi.org/10.1190/GEO2015-0402.1)

566 Gleeson, T., Wada, Y., Bierkens, M. F. P., & Van Beek, L. P. H. (2012). Water balance of global
567 aquifers revealed by groundwater footprint. *Nature*, 488(7410), 197–200.

568 Gottlieb, J., & Dietrich, P. (1995). Identification of the permeability distribution in soil by
569 hydraulic tomography. *Inverse Problems*, 11(2), 353.

570 Guglielmi, Y., Nussbaum, C., Jeanne, P., Rutqvist, J., Cappa, F., & Birkholzer, J. (2020).
571 Complexity of Fault Rupture and Fluid Leakage in Shale: Insights From a Controlled Fault
572 Activation Experiment. *Journal of Geophysical Research: Solid Earth*, 125(2),
573 e2019JB017781. <https://doi.org/10.1029/2019JB017781>

574 Hochstetler, D. L., Barrash, W., Leven, C., Cardiff, M., Chidichimo, F., & Kitanidis, P. K. (2016).
575 Hydraulic tomography: Continuity and discontinuity of high-K and low-K zones.
576 *Groundwater*, 54(2), 171–185.

577 Horiguchi, Y. (1998). Outline of water-dissolved natural gas field in Chiba Prefecture. *Journal of*
578 *the Japanese Association for Petroleum Technology*, 63(6), 475–484.
579 <https://doi.org/10.3720/japt.63.475>

580 Huntley, D. (1986). Relations between permeability and electrical resistivity in granular aquifers.
581 *Groundwater*, 24(4), 466–474.

582 Hsieh, P. A., Bredehoeft, J. D., & Farr, J. M. (1987). Determination of aquifer transmissivity from
583 Earth tide analysis. *Water Resources Research*, 23(10), 1824–1832.

584 Istok, J. D., & Dawson, K. J. (2014). *Aquifer testing: design and analysis of pumping and slug*

585 *tests*. CRC Press.

586 Jardani, A., and A. Revil (2009), Stochastic joint inversion of temperature and self-potential data,
587 *Geophys. J. Int.*, 179(1), 640– 654, doi:10.1111/j.1365-246X.2009.04295.x.

588 Jha, B., Bottazzi, F., Wojcik, R., Coccia, M., Bechor, N., McLaughlin, D., et al. (2015). Reservoir
589 characterization in an underground gas storage field using joint inversion of flow and
590 geodetic data. *International Journal for Numerical and Analytical Methods in*
591 *Geomechanics*, 39(14), 1619–1638.

592 Jiang, G., Qiao, X., Wang, X., Lu, R., Liu, L., Yang, H., et al. (2020). GPS observed horizontal
593 ground extension at the Hutubi (China) underground gas storage facility and its application
594 to geomechanical modeling for induced seismicity. *Earth and Planetary Science Letters*,
595 530, 115943. [https://doi.org/https://doi.org/10.1016/j.epsl.2019.115943](https://doi.org/10.1016/j.epsl.2019.115943)

596 Jiménez, S., Brauchler, R., Hu, R., Hu, L., Schmidt, S., Ptak, T., & Bayer, P. (2015). Prediction of
597 solute transport in a heterogeneous aquifer utilizing hydraulic conductivity and specific
598 storage tomograms. *Water Resources Research*, 51(7), 5504–5520.

599 Jones, D. R., Schonlau, M., & Welch, W. J. (1998). Efficient global optimization of expensive
600 black-box functions. *Journal of Global Optimization*, 13(4), 455–492.

601 Jousset, P., Reinsch, T., Ryberg, T., Blanck, H., Clarke, A., Aghayev, R., et al. (2018). Dynamic
602 strain determination using fibre-optic cables allows imaging of seismological and structural
603 features. *Nature Communications*, 9(1). <https://doi.org/10.1038/s41467-018-04860-y>

604 Keranen, K. M., Weingarten, M., Abers, G. A., Bekins, B. A., & Ge, S. (2014). Sharp increase in
605 central Oklahoma seismicity since 2008 induced by massive wastewater injection. *Science*,
606 345(6195), 448–451. <https://doi.org/10.1126/science.1255802>

607 Kishida, K., Yamauchi, Y., & Guzik, A. (2014). Study of optical fibers strain-temperature
608 sensitivities using hybrid Brillouin-Rayleigh System. *Photonic Sensors*, 4(1), 1–11.

609 Kitanidis, P. K. (1997). *Introduction to geostatistics: applications in hydrogeology*. Cambridge

- 610 university press.
- 611 Lei, X., Xue, Z., & Hashimoto, T. (2019). Fiber optic sensing for geomechanical monitoring:(2)-
612 distributed strain measurements at a pumping test and geomechanical modeling of
613 deformation of reservoir rocks. *Applied Sciences*, 9(3), 417.
- 614 Lei, X., Su, J., & Wang, Z. (2020). Growing seismicity in the Sichuan Basin and its association
615 with industrial activities. *Science China Earth Sciences*, 1–28.
- 616 Liang, L., Abubakar, A., & Habashy, T. M. (2016). Reservoir property mapping and monitoring
617 from joint inversion of time-lapse seismic, electromagnetic, and production data.
618 *Geophysics*, 81(5), ID73–ID84.
- 619 Maldaner, C. H., Munn, J. D., Coleman, T. I., Molson, J. W., & Parker, B. L. (2019).
620 Groundwater Flow Quantification in Fractured Rock Boreholes Using Active Distributed
621 Temperature Sensing Under Natural Gradient Conditions. *Water Resources Research*, 55(4),
622 3285–3306. <https://doi.org/10.1029/2018WR024319>
- 623 Medina, R., Pham, C., Plumlee, M. H., Hutchinson, A., Becker, M. W., & O’Connell, P. J.
624 (2020). Distributed temperature sensing to measure infiltration rates across a groundwater
625 recharge basin. *Groundwater*, n/a(n/a). <https://doi.org/10.1111/gwat.13007>
- 626 Menke, W. (2018). *Geophysical data analysis: Discrete inverse theory*. Academic press.
- 627 Miller, M. M., Shirzaei, M., & Argus, D. (2017). Aquifer Mechanical Properties and Decelerated
628 Compaction in Tucson, Arizona. *Journal of Geophysical Research: Solid Earth*, 122(10),
629 8402–8416. <https://doi.org/10.1002/2017JB014531>
- 630 Murdoch, L. C., Germanovich, L. N., DeWolf, S. J., Moysey, S. M. J., Hanna, A. C., Kim, S., &
631 Duncan, R. G. (2020). Feasibility of using in situ deformation to monitor CO2 storage.
632 *International Journal of Greenhouse Gas Control*, 93(September 2018), 102853.
633 <https://doi.org/10.1016/j.ijggc.2019.102853>
- 634 Wilkins, A., Green, C.P., & Ennis-King, J. (2020). PoroFlow: a multiphysics simulation code

635 for coupled problems in porous media. *Journal of Open Source Software*, 5(55), 2176.

636 <https://doi.org/10.21105/joss.02176>

637 Ren, Z., & Kalscheuer, T. (2020). Uncertainty and resolution analysis of 2D and 3D inversion

638 models computed from geophysical electromagnetic data. *Surveys in Geophysics*, 41, 47–

639 112. <https://doi.org/10.1007/s10712-019-09567-3>

640 Rice, J. R., & Cleary, M. P. (1976). Some basic stress diffusion solutions for fluid-saturated

641 elastic porous media with compressible constituents. *Reviews of Geophysics*, 14(2), 227–

642 241.

643 Rucci, A., Vasco, D. W., & Novali, F. (2010). Fluid pressure arrival-time tomography: Estimation

644 and assessment in the presence of inequality constraints with an application to production at

645 the Krechba field, Algeria. *Geophysics*, 75(6), O39–O55.

646 Schenato, L. (2017). A review of distributed fibre optic sensors for geo-hydrological applications.

647 *Applied Sciences (Switzerland)*. <https://doi.org/10.3390/app7090896>

648 Shirzaei, M., Ellsworth, W. L., Tiampo, K. F., González, P. J., & Manga, M. (2016). Surface

649 uplift and time-dependent seismic hazard due to fluid injection in eastern Texas. *Science*,

650 353(6306), 1416–1419.

651 Shirzaei, M., Manga, M., & Zhai, G. (2019). Hydraulic properties of injection formations

652 constrained by surface deformation. *Earth and Planetary Science Letters*, 515, 125–134.

653 <https://doi.org/10.1016/j.epsl.2019.03.025>

654 Sun, Y., Xue, Z., Hashimoto, T., Lei, X., & Zhang, Y. (2020). Distributed Fiber Optic Sensing

655 System for Well-based Monitoring Water Injection Tests — A Geomechanical Responses

656 Perspective. *Water Resources Research*, 56, 1–30.

657 Vasco, D W. (2018). An extended trajectory mechanics approach for calculating the path of a

658 pressure transient: Derivation and illustration. *Water Resources Research*, 54(4), 2642–2660.

659 Vasco, D W, Datta-Gupta, A., & Long, J. C. S. (1997). Resolution and uncertainty in hydrologic

- 660 characterization. *Water Resources Research*, 33(3), 379–397.
- 661 Vasco, D W, Ferretti, A., & Novali, F. (2008). Reservoir monitoring and characterization using
662 satellite geodetic data: Interferometric synthetic aperture radar observations from the
663 Krechba field, Algeria. *Geophysics*, 73(6), WA113–WA122.
- 664 Vasco, D. W., & Mali, G. (2020). On the use of adjoints in the inversion of observed quasi-static
665 deformation. *Geophysical Journal International*, 224(2), 896–908.
666 <https://doi.org/10.1093/gji/ggaa481>
- 667 Vasco, D W, Rucci, A., Ferretti, A., Novali, F., Bissell, R. C., Ringrose, P. S., et al. (2010).
668 Satellite-based measurements of surface deformation reveal fluid flow associated with the
669 geological storage of carbon dioxide. *Geophysical Research Letters*, 37(3).
- 670 Vasco, D. W., Daley, T. M., & Bakulin, A. (2014). Utilizing the onset of time-lapse changes: A
671 robust basis for reservoir monitoring and characterization. *Geophysical Journal International*,
672 197(1), 542–556.
- 673 Vasco, Donald W, Doetsch, J., & Brauchler, R. (2019). An extended trajectory-mechanics
674 approach for calculating the path of a pressure transient: travel-time tomography. *Hydrology
675 and Earth System Sciences*, 23(11), 4541–4560.
- 676 Verdon, J. P., Stork, A. L., Bissell, R. C., Bond, C. E., & Werner, M. J. (2015). Simulation of
677 seismic events induced by CO2 injection at In Salah, Algeria. *Earth and Planetary Science
678 Letters*, 426, 118–129. <https://doi.org/https://doi.org/10.1016/j.epsl.2015.06.029>
- 679 Virtanen, P., Gommers, R., Oliphant, T. E., Haberland, M., Reddy, T., Cournapeau, D., et al.
680 (2020). SciPy 1.0: fundamental algorithms for scientific computing in Python. *Nature
681 Methods*, 17(3), 261–272.
- 682 Wang, C., Doan, M., Xue, L., & Barbour, A. J. (2018). Tidal response of groundwater in a leaky
683 aquifer—Application to Oklahoma. *Water Resources Research*, 54(10), 8019–8033.
- 684 Wang, H. F. (2017). *Theory of linear poroelasticity with applications to geomechanics and*

685 *hydrogeology*. Princeton University Press.

686 Yamamoto, T., Nye, T., & Kuru, M. (1995). Imaging the permeability structure of a limestone
687 aquifer by crosswell acoustic tomography. *Geophysics*, *60*(6), 1634–1645.

688 Yeh, T. J., & Liu, S. (2000). Hydraulic tomography: Development of a new aquifer test method.
689 *Water Resources Research*, *36*(8), 2095–2105.

690 Zhang, Y., & Xue, Z. (2019). Deformation–Based Monitoring of Water Migration in Rocks
691 Using Distributed Fiber Optic Strain Sensing: A Laboratory Study. *Water Resources*
692 *Research*, *55*(11), 8368–8383.

693 Zhang, Y., Xue, Z., Park, H., Shi, J., Kiyama, T., Lei, X., et al. (2019). Tracking CO₂ Plumes in
694 Clay–Rich Rock by Distributed Fiber Optic Strain Sensing (DFOSS): A Laboratory
695 Demonstration. *Water Resources Research*, *55*(1), 856–867.

696 Zhang, Y., Lei, X., Hashimoto, T., & Xue, Z. (2020). In situ hydromechanical responses during
697 well drilling recorded by distributed fiber-optic strain sensing. *Solid Earth Discussions*, 1–
698 15. <https://doi.org/10.5194/se-2020-61>